NANO LETTERS

pubs.acs.org/NanoLett Letter

Magnetic Field Magnitudes Needed for Skyrmion Generation in a General Perpendicularly Magnetized Film

Seungmo Yang, Tae-Seong Ju, Changsoo Kim, Hyun-Joong Kim, Kyongmo An, Kyoung-Woong Moon,* Sungkyun Park,* and Chanyong Hwang*

Cite This: *Nano Lett.* 2022, 22, 8430−8436 Read Online

ACCESS | Metrics & More | Article Recommendations | Supporting Information

ABSTRACT: Due to its topological protection, the magnetic skyrmion has been intensively studied for both fundamental aspects and spintronics applications. However, despite recent advancements in skyrmion research, the deterministic creation of isolated skyrmions in a generic perpendicularly magnetized film is still one of the most essential and challenging techniques. Here, we present a method to create magnetic skyrmions in typical perpendicular magnetic anisotropy (PMA) films by applying a magnetic field pulse and a method to determine the magnitude of the required external magnetic fields. Furthermore, to demonstrate the usefulness of this result for future skyrmion research, we also experimentally study the PMA dependence on the minimum size of skyrmions. Although field-driven skyrmion generation is unsuitable for device application, this result can provide an easier approach for obtaining isolated skyrmions, making skyrmion-based research more accessible.

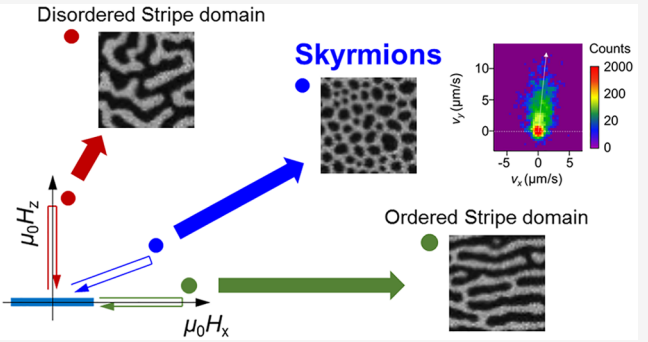

KEYWORDS: *skyrmion, spintronics, perpendicular magnetic anisotropy, skyrmion generation*

A magnetic skyrmion is a particle-like topological spin texture with the ±1 skyrmion charge, defined by $\frac{1}{4\pi}\iint \mathbf{m}\cdot(\partial_x\mathbf{m}\times\partial_y\mathbf{m})\,dx\,dy$, where $\mathbf{m}(x, y)$ is a unit magnetization vector.[1] It has been extensively studied in the magnetism research field due to its unique physical properties, such as topologically protected stability,[2,3] nanoscale size,[4−6] and extremely low current for electrical manipulation.[7−11] As a result of the topological features, several novel physical phenomena, such as the skyrmion Hall effect[12−14] and topological Hall effect,[15−19] have also been experimentally observed. Starting from the experimental observation of room-temperature isolated skyrmions, various skyrmion-based spintronic devices, such as memory devices,[20−24] logic devices,[25−28] and neuromorphic devices,[29−33] have also been proposed.[10,34] As such, for fundamental research and spintronics application, it is essential to obtain a stable skyrmion.

However, it has been a significant practical issue in skyrmion research to stabilize isolated magnetic skyrmions at room temperature. The isolated skyrmion in a perpendicularly magnetized system is stabilized only when several material parameters, such as the perpendicular magnetic anisotropy (PMA), the magnetic dipole interaction ($\mu_0 M_S^2$), and the Dzyaloshinskii−Moriya interaction (DMI), meet a particular ratio.[35,36] In some studies, a complex multilayer structure with more than ten repeated numbers was adopted to enhance $\mu_0 M_S^2$,[10,11,37] or extremely fine interface engineering was used to adjust PMA.[24,28] Moreover, even if an optimized material to stabilize a Neel-type skyrmion is obtained, deterministic skyrmion generation is also tricky. Previous works reported the generation of isolated skyrmions using an external magnetic field,[36,38−40] spin-polarized electric current,[8,34] or thermal energy.[41−43] However, the reported approaches are accompanied by a complicated patterning process to induce nonuniform spin-torque[9] or a specific device geometry, laser, or heating holder to inject localized heat.[41,42] For example, while Woo et al.[44] reported reliable current-induced generation or annihilation of an isolated magnetic skyrmion, the underlying mechanism is based on unintended defects. As another example, Finizio et al.[45] presented a creative device structure that can nucleate and delete an isolated magnetic skyrmion using an electrical signal, but the device geometry is quite complicated. In this sense, to promote extensive skyrmion research, a universal method for generating skyrmions in a general PMA sample is required.

Received: June 6, 2022
Revised: October 8, 2022
Published: October 25, 2022

https://doi.org/10.1021/acs.nanolett.2c02268
Nano Lett. 2022, 22, 8430−8436

Recent work demonstrated deterministic isolated skyrmion creation in a typical PMA sample at zero magnetic field after applying a magnetic field pulse at a particular angle.[36] Here, a method to quantitatively determine the magnitude of the required external magnetic fields for skyrmion creation is investigated. The external magnetic field pulse amplitudes for skyrmion generation in various PMA samples are derived theoretically and demonstrated experimentally. It is expected that the proposed technique for generating skyrmions in a generic PMA film will make future skyrmion-related studies relatively easier to conduct than before. To prove the usefulness of our method for skyrmion research, we present the PMA dependence on skyrmion size variation by the z-axis external magnetic field and its minimum size, which has never been experimentally investigated because of the difficulty to obtain stabilized skyrmions in various PMA samples.

Domain States at Zero Magnetic Field after Applying a Magnetic Field Pulse. We studied sample stacks of Si/SiO_2/W (50 Å)/$Co_{20}Fe_{60}B_{20}$ (13 Å)/Ta (1.072 Å)/MgO (10 Å)/Ta (30 Å) with PMA, where an ultrathin Ta layer was inserted to control the strength of the PMA because PMA originates from the interface between the CoFeB and MgO layers.[46,47] Considering the effective PMA field (H_k), defined by the equation $K_{eff} = \frac{\mu_0 M_S H_k}{2}$, where K_{eff} is the effective PMA energy per volume and M_S is the saturation magnetization, $\mu_0 H_k$ was determined as 70.4 mT (see Supporting Information 1). It was recently reported that diverse stripe and bubble domain patterns were formed after simultaneously applying pulses of x- and z-axis magnetic fields,[36] where the z-axis is the film's normal direction and the x-axis is an arbitrary direction on the film plane. Therefore, to provide the quantitative condition of the applied external magnetic field for skyrmion domain (SkD) formation, we investigated the domain pattern change after various combinations of simultaneous x- and z-axis magnetic field pulses (Figure 1a). All magnetic domain images were taken using a polar magneto-optical Kerr effect (MOKE) microscope system, where the light gray (dark gray) color represents the $+z$ ($-z$) magnetization. The initial state was set as a half-filled stripe domain pattern with rotational symmetry about the z-axis (Figure 1b). The initial state can be formed by applying only a z-axis magnetic field (H_z) pulse of sufficient magnitude (the red arrow in Figure 1a) because the z-axis magnetic field cannot break symmetry in the film plane. The stripe domain in Figure 1b is denoted as a disordered stripe (DS) domain. The corresponding fast Fourier transformation (FFT) image (Figure 1e) has a circular shape, indicating a rotational symmetry of the stripe domain in the film plane. By contrast, after the simultaneous application of x- and z-axis magnetic field pulses (the blue arrow in Figure 1a), SkDs were created (Figure 1c). The close-packed skyrmion state in Figure 1c is denoted as a SkD. We also observed that the generated magnetic bubbles are well shifted by spin orbit torque (SOT) as presented in Figure 1j–k. Here, we controlled the skyrmion density to obtain isolated skyrmions by applying a perpendicular magnetic field (see Supporting Information 2). In the static MOKE image (Figure 1c), it cannot be distinguished whether the circular-shaped domains are skyrmions or not. One helpful approach to determine if the generated circular domain is a skyrmion is to observe the skyrmion Hall effect.[12,13,48] The skyrmion texture of the circular domains in Figure 1c has been verified by observing the skyrmion Hall angle of 9° with the current direction as

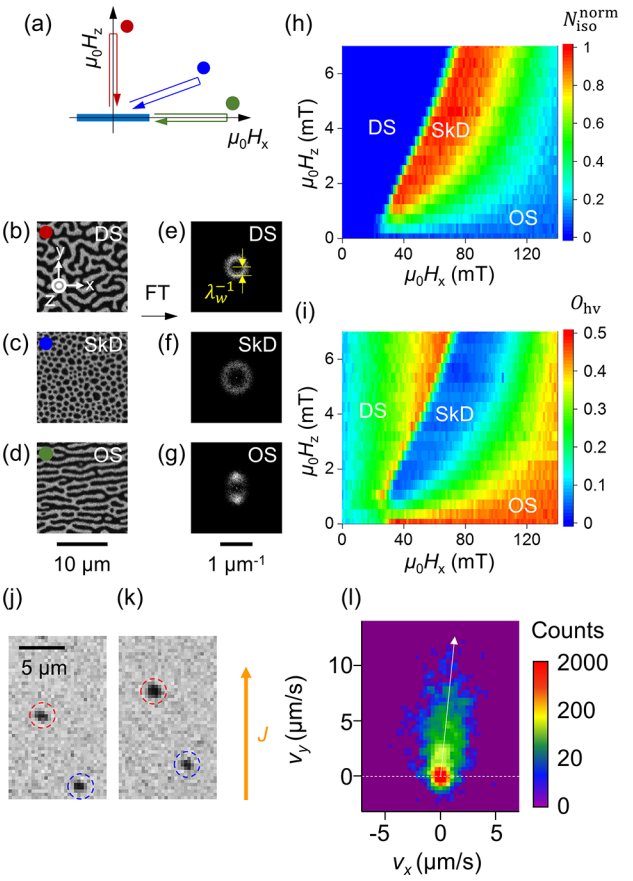

Figure 1. Various magnetic domain structures formed by external magnetic fields. (a) Schematic illustration for applications of external magnetic field pulses to form magnetic domain patterns. (b, c, d) Representative magnetic domain images after magnetic field pulse application along (b) red, (c) blue, and (d) green arrows in panel a. (e, f, g) Corresponding Fourier transformation (FT) images of the magnetic domain for (e) disordered stripe, (f) skyrmion domain, and (g) ordered stripe. (h) Experimental mapping of the normalized number (N_{iso}^{norm}) of isolated domains after applying x- and z-axis external magnetic field pulses of varying magnitude. (i) Experimental mapping result of the orientational order parameter (O_{hv}). (j, k) Sequential MOKE images demonstrating the spin–orbit torque (SOT)-driven motion of isolated skyrmions after applying electric current pulses of 100 ms with an amplitude $J = 7.5 \times 10^{-8}$ A/m^2 under the z-axis external magnetic field ($\mu_0 H_z$ = 1.1 mT). (l) Measurement of the skyrmion Hall angle.

shown in Figure 1 (see Supporting Information 3 for a more detailed explanation for analysis). The corresponding FFT image of the SkD in Figure 1f is also circular. Lastly, an aligned stripe domain pattern along the x-axis was obtained by applying only the x-axis magnetic field (H_x) pulse (Figure 1d), where the rotational symmetry is broken about the z-axis because the application of H_x breaks the symmetry by lowering the energy of the x-component magnetization. Likewise, the aligned stripe domain pattern along the x-axis of Figure 1d is denoted as an ordered stripe (OS) domain. Significantly, the corresponding FFT image of the OS in Figure 1g shows two clear spots along the transverse direction of the aligned domain, which means constant repetition of stripe domains along the transverse direction.

To further investigate the magnetic field pulse dependence on the consequent domain patterns, we mapped the normalized number of isolated domains (N_{iso}^{norm}) in a defined

https://doi.org/10.1021/acs.nanolett.2c02268
Nano Lett. 2022, 22, 8430–8436

region. All isolated domains were counted regardless of polarity (the domains attached to the image boundary of the defined region were excluded). For example, the number of isolated domains (N_{iso}) for the DS in Figure 1b is zero because all of the domains are attached to the boundary. For the SkD of Figure 1c, N_{iso} is very large because there are many isolated dark gray domains. N_{iso} of the OS is small because there are a few isolated domains regardless of the domain polarity (Figure 1d). The values of N_{iso} are normalized by the maximum N_{iso} in the SkD. The mapping is presented in Figure 1h. This mapping clearly distinguishes between the two stripe domains (DS + OS) and SkD as blue and red regions, respectively. However, it is not able to separate between DS and OS. To also classify the DS and the OS, we introduced an orientational order parameter as[49]

$$O_{hv} \equiv \left| \frac{n_h - n_v}{n_h + n_v} \right| \quad (1)$$

where n_h (n_v) is the number of horizontal (vertical) pairs of nearest neighbor spins with antiparallel perpendicular components. For example, in DS and SkD, n_v and n_h are almost equal, due to the rotational symmetry, leading to a small value of O_{hv}. However, in OS, n_v is much larger than n_h because of the horizontally aligned shape of domains, resulting in the larger value of O_{hv}. It allows us to classify the two rotationally symmetric DS/SkD and the asymmetric OS (Figure 1i). Therefore, we can distinguish three types of domain patterns by comparing the two parameters of N_{iso}^{norm} and O_{hv}. Here, we can observe a high O_{hv} region at the boundary between DS and SkD. This is the aligned stripe domain state due to a slightly small amplitude of the in-plane field to reach a critical stripe domain width (see Supporting Information 4). The domain pattern is highly dependent on the magnitude of the pulses of the x- and z-axis magnetic fields (Figure 1h,i). To form a SkD, the particular magnitudes of the magnetic field pulses of the x- and z-axes must be selected. This work aims to provide a helpful approach for selecting the particular magnetic field magnitudes to generate the SkD in generic PMA films.

Perpendicular Magnetic Anisotropy Dependence on Domain Pattern Formation. First, we investigated the dependence of the PMA on domain pattern formation. To obtain various PMA samples with other material parameters fixed, we changed the thickness of the Ta insertion layer (Figure 2a). Even a slight change in the Ta layer thickness from 1.067 to1.076 Å significantly affected the stripe domain width (λ_0) (Figure 2b–e) (see Supporting Information 5 for a detailed explanation for the ultrathin thickness control). The values of $\mu_0 H_k$ and λ_0 as a function of the Ta layer thickness are presented in Figure 2f. The stripe domain width as a function of PMA is written as[39]

$$\lambda_0 \cong \pi \Delta_w \, e^{(1+\pi\sigma_w/(\mu_0 M_s^2 d))} \quad (2)$$

where Δ_w is a typical domain wall width, μ_0 is the magnetic permeability, d is the thickness of the ferromagnetic layer, and σ_w is the domain wall energy density per area, which is mainly proportional to $\sqrt{H_k}$. Figure 2g shows a linear relation between $\sqrt{H_k}$ and ln λ_0, verifying the validity of eq 2.

Next, the same mapping analysis as in Figure 1h,i was performed on various PMA samples using a magnetic field pulse of 1000 ms. Figure 3 presents representative mapping

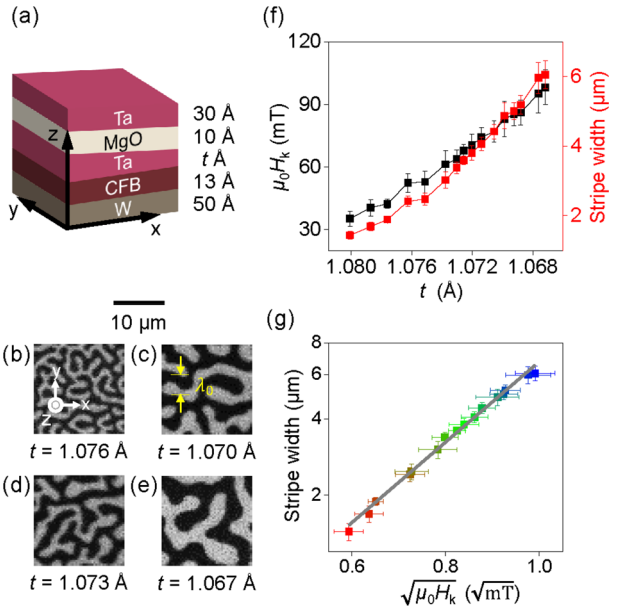

Figure 2. Magnetic properties and corresponding stripe domain patterns. (a) Schematic of the sample structure where the Ta layer is inserted between the CoFeB and MgO layers. (b–e) Magnetic stripe domain images obtained with MOKE microscope at zero magnetic field. t is the inserted Ta nominal thickness. (f) Magnetic anisotropy field and the stripe domain width according to the Ta insertion layer thickness. Error bars were determined from 10 measurements in a 20 × 70 μm^2 region. (g) Stripe domain width as a function of PMA. The solid gray line is a linear fitting line of the measured data, where the error bar is the standard deviation from panel f.

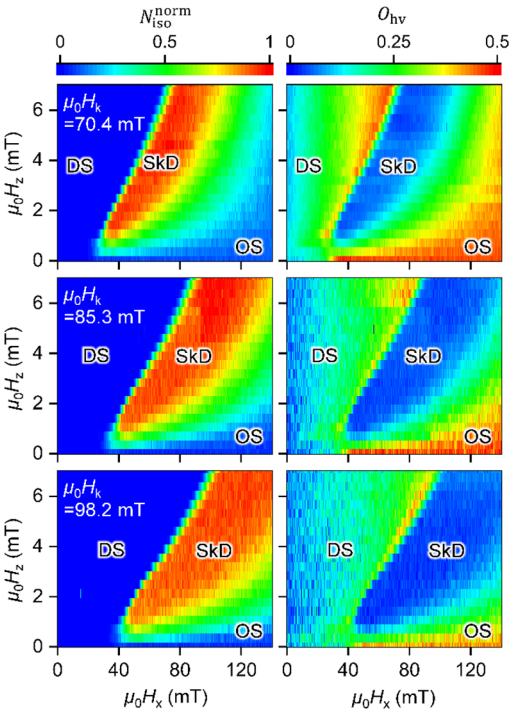

Figure 3. Dependence of PMA on magnetic domain pattern changes. Representative experimental mapping data of (left) N_{iso}^{norm} and (right) O_{hv} obtained by modulating the magnitude of x- and z-axis external magnetic field pulses for the samples having $\mu_0 H_k$ values of 70.4 mT, 85.3 mT, and 98.2 mT.

https://doi.org/10.1021/acs.nanolett.2c02268
Nano Lett. 2022, 22, 8430−8436

results for the samples having $\mu_0 H_k$ = 70.4 mT, 85.3 mT, and 98.2 mT samples. The overall shapes of the region for the SkD are similar to each other for diverse H_k samples, but two main things are changed: the region for the SkD expands with an increase in H_k, and the minimum H_x to form a SkD also increases with an increase in H_k. Because the particular x- and z-axis magnetic fields to form the SkD depend on PMA (H_k), a universal approach to determine the magnetic fields is required regardless of PMA.

A recent study on the transition between uniform, stripe and SkDs demonstrated that the SkD can always be the global minimum energy state by applying an appropriate perpendicular magnetic field regardless of PMA or stripe width.[50] However, when the stripe width is larger than a specific critical value, the stripe-to-SkD transition does not occur at room temperature even though the SkD is the global minimum energy state.[50] This is because the stripe-to-SkD transition occurs by thermal fluctuation. Because of the thermal energy, the domain walls randomly fluctuate back and forth from their equilibrium position. Then, when two adjacent domain walls collide, a stripe domain could be cut into a bubble domain. Therefore, the collision probability is inversely proportional to the distance between two domain walls, which corresponds to the stripe width. Hence, the stripe-to-SkD transition at room temperature occurs when the stripe width is smaller than a certain critical value. Application of H_x reduces the stripe width, which means that there exists a specific H_x to stabilize the critical stripe domain width (λ_c), where the stripe domains start to be cut.[51] To determine the critical stripe domain width in our system, we investigated N_{iso}^{norm} after applying H_x pulses of various magnitudes, starting from the initial DS state (N_{iso}^{norm} = 0). N_{iso}^{norm} presents a sharp increase at a particular H_x, marked with black arrows in Figure 4a, and the magnitude of H_x is dependent on the PMA (the numbers in Figure 4a,b are values of $\mu_0 H_k$). To explain the detailed dependence, the stripe domain width change was observed under applied H_x as a function of the magnitude (Figure 4b). The black circles in Figure 4b indicate the values of the sharply increasing points in Figure 4a. All the black circles indicate almost the same value of the stripe domain width, about 1.5 μm. That is, for all different PMA samples, N_{iso}^{norm} starts to increase (or stripe domains start to be cut) when the stripe domain width becomes smaller than the λ_c of 1.5 μm. Therefore, the results allow us to infer that the minimum $\mu_0 H_x$ to form a SkD in Figure 3 is the value of $\mu_0 H_x$ required to stabilize the critical stripe domain width of 1.5 μm. Furthermore, recent work[51] reported that the stripe domain width change for various PMA samples could be scaled by H_x/H_k. Then, because the critical stripe domain width is almost identical regardless of PMA (Figure 4b), the minimum H_x to form a SkD is a function of H_k. Therefore, we normalized the x-axis of the N_{iso}^{norm} mapping graphs by H_x/H_k as shown in Figure 4c, where the curves were obtained from the N_{iso}^{norm} = 0.85 lines from the normalized mapping graphs of various PMA samples. All the lines of N_{iso}^{norm} = 0.85 are collapsed regardless of PMA, indicating that the stripe domain width scaled by H_x/H_k is the main parameter for generating a SkD, irrespective of PMA.

To derive the quantitative model to determine the minimum H_x to form a SkD, we used eq 2 and a simple linear Zeeman energy by H_x as follows:

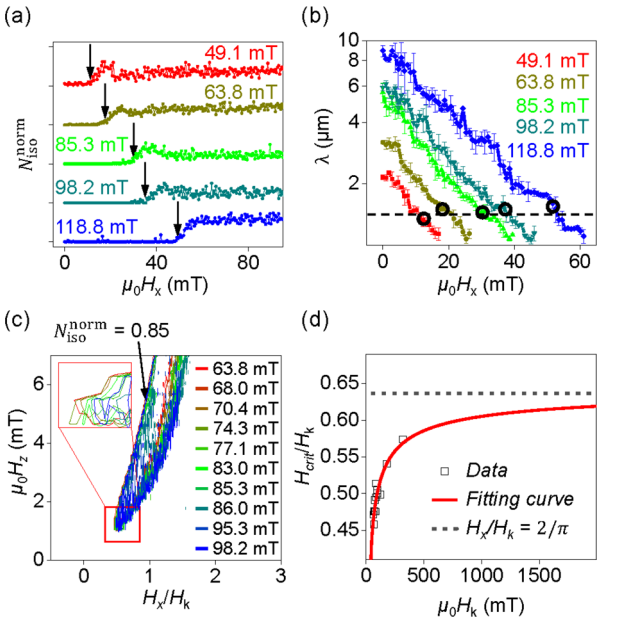

Figure 4. Effect of $\mu_0 H_x$ on magnetic domain patterns and variation in the critical magnetic field for skyrmion generation. (a) Value of N_{iso}^{norm} after applying x-axis magnetic field ($\mu_0 H_x$) pulse. The numbers above the curves indicate the $\mu_0 H_k$. Black arrows are marked at the sharply increasing point for each curve. (b) Stripe domain width under $\mu_0 H_x$. Black circles represent the $\mu_0 H_x$ value indicated by the black arrows in respective data in panel a. A black dashed line shows the λ value of 1.5 μm. (c) Curves of the N_{iso}^{norm} value of 0.85 for various $\mu_0 H_k$ samples. The inset presents an enlarged image of the boundaries. The left-most edges of curves are chosen as the critical magnetic field ($\mu_0 H_{crit}$) for creating skyrmions. (d) Change of H_{crit}/H_k as a function of $\mu_0 H_k$. Black squares indicate measured data, and the red line is a fitting line of eq 4. The black dashed line indicates the value of $2/\pi$.

$$\lambda_c = \pi \Delta_w \, e^{(1+\pi\sigma_w/(\mu_0 M_s^2 d))};$$
$$\sigma_w \cong 4\sqrt{AK_{eff}} - \pi \Delta_w \mu_0 M_S H_{crit} \quad (3)$$

where A is the exchange stiffness and H_{crit} is the minimum H_x to induce λ_c. The $\pi\Delta_w \mu_0 M_S H_{crit}$ term indicates the domain wall energy generated by the Zeeman energy. It is also assumed that H_{crit} is larger than the DMI field so that the magnetizations in the domain walls are aligned to the H_{crit} direction. Here, we are also dealing with the ordered stripe domain along the in-plane direction due to a sufficiently large in-plane magnetic field. Considering that the change in the stripe domain width can be scaled by H_x/H_k, we can rearrange eq 3 for H_{crit}/H_k as

$$\frac{H_{crit}}{H_k} = \frac{2}{\pi} - \left[\frac{M_s d\sqrt{\mu_0 M_s/2}}{\pi^2\sqrt{A}} \ln\left(\frac{\lambda_c}{\pi e \Delta_w}\right)\right]\frac{1}{\sqrt{H_k}} \quad (4)$$

where we already know that λ_c is about 1.5 μm. Equation 4 indicates that with a sufficiently large H_k, the value of H_{crit}/H_k converges to $2/\pi$. The values of H_{crit}/H_k for various PMAs obtained from Figure 4c are presented in Figure 4d as black squares, and the points are well-fitted by eq 4 (described as a solid red line). In this approach, the role of DMI is described in more detail in Supporting Information 6. Therefore, the minimum x-axis magnetic field (H_{crit}) to form a SkD can be obtained from eq 4 provided that all material parameters for general PMA samples are known.

https://doi.org/10.1021/acs.nanolett.2c02268
Nano Lett. 2022, 22, 8430−8436

Using eq 4, we can calculate the specific critical value of $\mu_0 H_x$ to cut the stripe domain for each PMA sample with several material parameters. The calculated values of $\mu_0 H_{crit}$ for the $\mu_0 H_k$ = 40.5 mT, 52.9 mT, 68.0 mT, 83.0 mT, and 98.2 mT samples were 14.7 mT, 21.0 mT, 29.0 mT, 37.0 mT, and 45.3 mT, respectively. Here, we used M_s of 900 emu/cm^3, A of 1.0×10^{-11} J/m, and Δ_w of 50 nm. When the magnetic field pulse magnitude of $\mu_0 H_x$ is larger than $\mu_0 H_{crit}$ and the z-axis pulse is appropriately adjusted, the SkD is stabilized (Figure 5a). The $\mu_0 H_{crit}$ values calculated above are marked as the empty stars in Figure 5a. To verify these critical values experimentally, we arbitrarily selected specific points inside the SkD region as marked with the solid stars. The representative SkD images are provided in the insets of Figure 5a, where the numbers in the boxes indicate the PMA strengths ($\mu_0 H_k$). Furthermore, it was confirmed that the SkD is also generated by the magnetic field pulses of other points inside the curve in Figure 5a, where the specific form of the SkD is identical (see Supporting Information 7). This result demonstrated an effective method for determining the x- and z-axis magnetic field pulse magnitudes for obtaining a SkD in an arbitrary PMA sample.

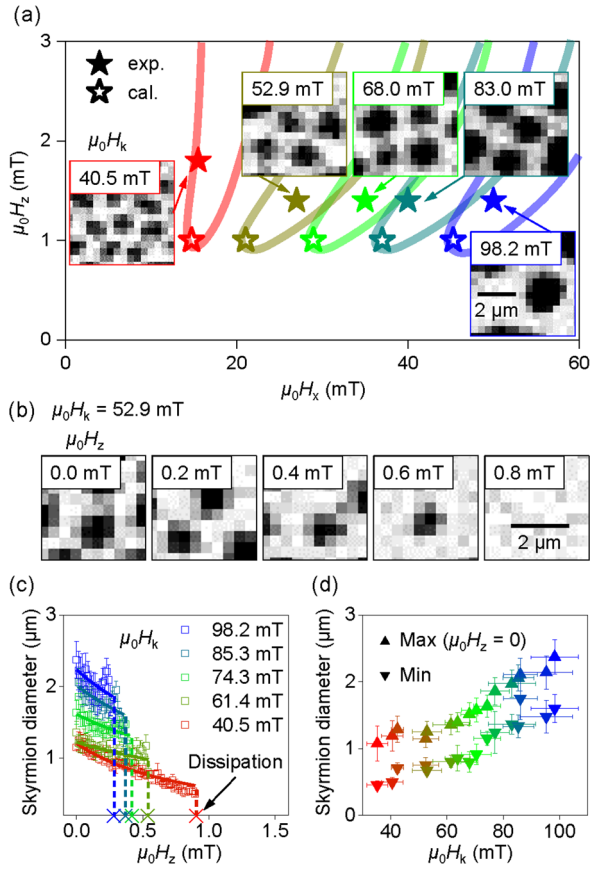

Figure 5. Skyrmion size change under z-axis external magnetic fields. (a) Deterministic generation of skyrmions for the samples with diverse PMA energy. Inset, MOKE images of SkDs created by the magnetic pulses of the specific points (solid stars), where the numbers indicate the respective $\mu_0 H_k$ value. The calculated critical magnetic fields are marked as empty stars. (b) MOKE images under the z-axis external magnetic field ($\mu_0 H_z$) for the $\mu_0 H_k$ = 52.9 mT sample, where the numbers in the images indicate the magnitude of $\mu_0 H_z$. (c) Variation in skyrmion diameter by the $\mu_0 H_z$ for diverse $\mu_0 H_k$ samples, where the colored solid lines are fitted by $1/(A \times \mu_0 H_z + B)$. The X marks indicate the magnitude of $\mu_0 H_z$ for skyrmion dissipation. (d) Range of skyrmion diameter as a function of PMA.

Determining the required magnetic field magnitude for skyrmion generation can provide a platform for investigating skyrmion properties in diverse material parameters. For example, we investigated the skyrmion size variation as a function of the z-axis external magnetic field. First, the size of the skyrmions at zero magnetic field increases as $\mu_0 H_k$ increases (Figure 5a), consistent with previous works.[48] Furthermore, the skyrmion size was reduced by applying a z-axis external magnetic field pointing in the opposite direction of the skyrmion core polarity. This is because the z-axis external magnetic field favors a wider magnetization domain parallel to the field direction. Figure 5b shows the z-axis external magnetic field dependence of the skyrmion size for the $\mu_0 H_k$ = 52.9 mT sample (see Supporting Information 8 for a detailed method to precisely determine skyrmion size). The diameter of the skyrmions decreases from about 1.2 μm to 0.8 μm with increasing $\mu_0 H_z$. Additionally, when the z-axis external magnetic field was larger than the critical perpendicular magnetic field, the skyrmions completely dissipated instead of becoming much smaller. To investigate the correlation between size, dissipation, and $\mu_0 H_k$, we plotted the z-axis external magnetic field dependent size of the skyrmions in the different PMA samples as summarized in Figure 5c. First, the size of the skyrmions was inversely proportional to the z-axis external magnetic field, and the decrease in size was well fitted[52] by $1/(A \times \mu_0 H_z + B)$ (solid color lines in Figure 5c). Second, the critical perpendicular magnetic field to dissipate skyrmions decreased when the PMA energy increased (solid X marks in Figure 5c). The decrease in the critical field for dissipation is because the critical field is inversely proportional to the stripe width at zero magnetic field.[39,53] From the above result, we can acquire the stable skyrmion size range between the minimum and maximum size for all samples (Figure 5d). This result can provide a guideline for designing the material parameters for skyrmion-based device applications or studies, verifying the usefulness of the proposed skyrmion generation method.

In conclusion, we presented a method for determining the required x- and z-axis magnetic field magnitudes to generate skyrmions for arbitrary PMA films. The equation was derived by clearly understanding the phase transition between the stripe domain states and SkD states. Thus, we successfully proved that the SkD could be generated by H_x of approximately 64% ($2/\pi$) of H_k in general PMA films. Using this method, we could easily investigate skyrmion behavior with various material parameters without adopting complicated techniques such as a complex multilayer or extremely fine thickness control.

■ ASSOCIATED CONTENT

Supporting Information

The Supporting Information is available free of charge at https://pubs.acs.org/doi/10.1021/acs.nanolett.2c02268.

Determination of the PMA, skyrmion density control, detailed analysis of the presence of the skyrmion Hall effect, validity of the ultrathin Ta thickness control, the role of DMI, Method to evaluate skyrmion size (PDF)

https://doi.org/10.1021/acs.nanolett.2c02268
Nano Lett. 2022, 22, 8430−8436

AUTHOR INFORMATION

Corresponding Authors

Kyoung-Woong Moon − *Quantum Spin Team, Korea Research Institute of Standards and Science, Daejeon 34113, Republic of Korea*; Email: kwmoon@kriss.re.kr

Sungkyun Park − *Department of Physics, Pusan National University, Busan 46241, Republic of Korea*; orcid.org/0000-0003-1816-310X; Email: psk@pusan.ac.kr

Chanyong Hwang − *Quantum Spin Team, Korea Research Institute of Standards and Science, Daejeon 34113, Republic of Korea*; orcid.org/0000-0002-6612-7552; Email: cyhwang@kriss.re.kr

Authors

Seungmo Yang − *Quantum Spin Team, Korea Research Institute of Standards and Science, Daejeon 34113, Republic of Korea*

Tae-Seong Ju − *Quantum Spin Team, Korea Research Institute of Standards and Science, Daejeon 34113, Republic of Korea; Department of Physics, Pusan National University, Busan 46241, Republic of Korea*

Changsoo Kim − *Quantum Spin Team, Korea Research Institute of Standards and Science, Daejeon 34113, Republic of Korea*

Hyun-Joong Kim − *Quantum Spin Team, Korea Research Institute of Standards and Science, Daejeon 34113, Republic of Korea*

Kyongmo An − *Quantum Spin Team, Korea Research Institute of Standards and Science, Daejeon 34113, Republic of Korea*

Complete contact information is available at: https://pubs.acs.org/10.1021/acs.nanolett.2c02268

Author Contributions

Seungmo Yang and Tae-Seong Ju contributed equally to this work.

Notes

The authors declare no competing financial interest.

ACKNOWLEDGMENTS

This study was supported by the National Research Foundation of Korea [Grant Nos. NRF-2021M3F3A2A01037663 and NRF-2022M3H4A1A04071154].

REFERENCES

(1) Nagaosa, N.; Tokura, Y. Topological properties and dynamics of magnetic skyrmions. *Nat. Nanotechnol.* **2013**, *8* (12), 899−911.

(2) Rossler, U. K.; Bogdanov, A. N.; Pfleiderer, C. Spontaneous skyrmion ground states in magnetic metals. *Nature* **2006**, *442* (7104), 797−801.

(3) Fert, A.; Reyren, N.; Cros, V. Magnetic skyrmions: advances in physics and potential applications. *Nat. Rev. Mater.* **2017**, *2* (7), 17031.

(4) Yu, X. Z.; Onose, Y.; Kanazawa, N.; Park, J. H.; Han, J. H.; Matsui, Y.; Nagaosa, N.; Tokura, Y. Real-space observation of a two-dimensional skyrmion crystal. *Nature* **2010**, *465* (7300), 901−904.

(5) Heinze, S.; von Bergmann, K.; Menzel, M.; Brede, J.; Kubetzka, A.; Wiesendanger, R.; Bihlmayer, G.; Blügel, S. Spontaneous atomic-scale magnetic skyrmion lattice in two dimensions. *Nat. Phys.* **2011**, *7* (9), 713−718.

(6) Romming, N.; Hanneken, C.; Menzel, M.; Bickel, J. E.; Wolter, B.; von Bergmann, K.; Kubetzka, A.; Wiesendanger, R. Writing and deleting single magnetic skyrmions. *Science* **2013**, *341* (6146), 636−639.

(7) Jonietz, F.; Muhlbauer, S.; Pfleiderer, C.; Neubauer, A.; Munzer, W.; Bauer, A.; Adams, T.; Georgii, R.; Boni, P.; Duine, R. A.; et al. Spin transfer torques in MnSi at ultralow current densities. *Science* **2010**, *330* (6011), 1648−1651.

(8) Sampaio, J.; Cros, V.; Rohart, S.; Thiaville, A.; Fert, A. Nucleation, stability and current-induced motion of isolated magnetic skyrmions in nanostructures. *Nat. Nanotechnol.* **2013**, *8* (11), 839−844.

(9) Iwasaki, J.; Mochizuki, M.; Nagaosa, N. Current-induced skyrmion dynamics in constricted geometries. *Nat. Nanotechnol.* **2013**, *8* (10), 742−747.

(10) Woo, S.; Litzius, K.; Kruger, B.; Im, M. Y.; Caretta, L.; Richter, K.; Mann, M.; Krone, A.; Reeve, R. M.; Weigand, M.; et al. Observation of room-temperature magnetic skyrmions and their current-driven dynamics in ultrathin metallic ferromagnets. *Nat. Mater.* **2016**, *15* (5), 501−506.

(11) Woo, S.; Song, K. M.; Han, H. S.; Jung, M. S.; Im, M. Y.; Lee, K. S.; Song, K. S.; Fischer, P.; Hong, J. I.; Choi, J. W.; et al. Spin-orbit torque-driven skyrmion dynamics revealed by time-resolved X-ray microscopy. *Nat. Commun.* **2017**, *8*, 15573.

(12) Jiang, W.; Zhang, X.; Yu, G.; Zhang, W.; Wang, X.; Benjamin Jungfleisch, M.; Pearson, J. E.; Cheng, X.; Heinonen, O.; Wang, K. L.; et al. Direct observation of the skyrmion Hall effect. *Nat. Phys.* **2017**, *13* (2), 162−169.

(13) Litzius, K.; Lemesh, I.; Krüger, B.; Bassirian, P.; Caretta, L.; Richter, K.; Büttner, F.; Sato, K.; Tretiakov, O. A.; Förster, J.; et al. Skyrmion Hall effect revealed by direct time-resolved X-ray microscopy. *Nat. Phys.* **2017**, *13* (2), 170−175.

(14) Litzius, K.; Leliaert, J.; Bassirian, P.; Rodrigues, D.; Kromin, S.; Lemesh, I.; Zazvorka, J.; Lee, K.-J.; Mulkers, J.; Kerber, N.; et al. The role of temperature and drive current in skyrmion dynamics. *Nat. Electron.* **2020**, *3* (1), 30−36.

(15) Neubauer, A.; Pfleiderer, C.; Binz, B.; Rosch, A.; Ritz, R.; Niklowitz, P. G.; Boni, P. Topological Hall effect in the A phase of MnSi. *Phys. Rev. Lett.* **2009**, *102* (18), 186602.

(16) Schulz, T.; Ritz, R.; Bauer, A.; Halder, M.; Wagner, M.; Franz, C.; Pfleiderer, C.; Everschor, K.; Garst, M.; Rosch, A. Emergent electrodynamics of skyrmions in a chiral magnet. *Nat. Phys.* **2012**, *8* (4), 301−304.

(17) Maccariello, D.; Legrand, W.; Reyren, N.; Garcia, K.; Bouzehouane, K.; Collin, S.; Cros, V.; Fert, A. Electrical detection of single magnetic skyrmions in metallic multilayers at room temperature. *Nat. Nanotechnol.* **2018**, *13* (3), 233−237.

(18) Zeissler, K.; Finizio, S.; Shahbazi, K.; Massey, J.; Ma'Mari, F. A.; Bracher, D. M.; Kleibert, A.; Rosamond, M. C.; Linfield, E. H.; Moore, T. A.; et al. Discrete Hall resistivity contribution from Neel skyrmions in multilayer nanodiscs. *Nat. Nanotechnol.* **2018**, *13* (12), 1161−1166.

(19) Kurumaji, T.; Nakajima, T.; Hirschberger, M.; Kikkawa, A.; Yamasaki, Y.; Sagayama, H.; Nakao, H.; Taguchi, Y.; Arima, T.-h.; Tokura, Y. Skyrmion lattice with a giant topological Hall effect in a frustrated triangular-lattice magnet. *Science* **2019**, *365* (6456), 914−918.

(20) Fert, A.; Cros, V.; Sampaio, J. Skyrmions on the track. *Nat. Nanotechnol.* **2013**, *8* (3), 152−156.

(21) Tomasello, R.; Martinez, E.; Zivieri, R.; Torres, L.; Carpentieri, M.; Finocchio, G. A strategy for the design of skyrmion racetrack memories. *Sci. Rep.* **2015**, *4*, 6784.

(22) Zhang, X.; Zhao, G. P.; Fangohr, H.; Liu, J. P.; Xia, W. X.; Xia, J.; Morvan, F. J. Skyrmion-skyrmion and skyrmion-edge repulsions in skyrmion-based racetrack memory. *Sci. Rep.* **2015**, *5*, 7643.

(23) Müller, J. Magnetic skyrmions on a two-lane racetrack. *New J. Phys.* **2017**, *19* (2), 025002.

(24) Yu, G.; Upadhyaya, P.; Shao, Q.; Wu, H.; Yin, G.; Li, X.; He, C.; Jiang, W.; Han, X.; Amiri, P. K.; et al. Room-Temperature Skyrmion Shift Device for Memory Application. *Nano Lett.* **2017**, *17* (1), 261−268.

https://doi.org/10.1021/acs.nanolett.2c02268
Nano Lett. 2022, 22, 8430−8436

(25) Zhang, X.; Ezawa, M.; Zhou, Y. Magnetic skyrmion logic gates: conversion, duplication and merging of skyrmions. *Sci. Rep.* **2015**, *5*, 9400.
(26) Xing, X.; Pong, P. W. T.; Zhou, Y. Skyrmion domain wall collision and domain wall-gated skyrmion logic. *Phys. Rev. B* **2016**, *94* (5), 054408.
(27) Luo, S.; Song, M.; Li, X.; Zhang, Y.; Hong, J.; Yang, X.; Zou, X.; Xu, N.; You, L. Reconfigurable Skyrmion Logic Gates. *Nano Lett.* **2018**, *18* (2), 1180−1184.
(28) Zazvorka, J.; Jakobs, F.; Heinze, D.; Keil, N.; Kromin, S.; Jaiswal, S.; Litzius, K.; Jakob, G.; Virnau, P.; Pinna, D.; et al. Thermal skyrmion diffusion used in a reshuffler device. *Nat. Nanotechnol.* **2019**, *14* (7), 658−661.
(29) Li, S.; Kang, W.; Huang, Y.; Zhang, X.; Zhou, Y.; Zhao, W. Magnetic skyrmion-based artificial neuron device. *Nanotechnology* **2017**, *28* (31), 31LT01.
(30) Huang, Y.; Kang, W.; Zhang, X.; Zhou, Y.; Zhao, W. Magnetic skyrmion-based synaptic devices. *Nanotechnology* **2017**, *28* (8), 08LT02.
(31) Bourianoff, G.; Pinna, D.; Sitte, M.; Everschor-Sitte, K. Potential implementation of reservoir computing models based on magnetic skyrmions. *AIP Adv.* **2018**, *8* (5), 055602.
(32) Song, K. M.; Jeong, J.-S.; Pan, B.; Zhang, X.; Xia, J.; Cha, S.; Park, T.-E.; Kim, K.; Finizio, S.; Raabe, J.; et al. Skyrmion-based artificial synapses for neuromorphic computing. *Nat. Electron.* **2020**, *3* (3), 148−155.
(33) Chen, R.; Li, C.; Li, Y.; Miles, J. J.; Indiveri, G.; Furber, S.; Pavlidis, V. F.; Moutafis, C. Nanoscale Room-Temperature Multilayer Skyrmionic Synapse for Deep Spiking Neural Networks. *Phys. Rev. Appl.* **2020**, *14* (1), 014096.
(34) Jiang, W.; Upadhyaya, P.; Zhang, W.; Yu, G.; Jungfleisch, M. B.; Fradin, F. Y.; Pearson, J. E.; Tserkovnyak, Y.; Wang, K. L.; Heinonen, O.; et al. Blowing magnetic skyrmion bubbles. *Science* **2015**, *349* (6245), 283−286.
(35) Bogdanov, A. N.; Panagopoulos, C. Physical foundations and basic properties of magnetic skyrmions. *Nat. Rev. Phys.* **2020**, *2* (9), 492−498.
(36) Moon, K.-W.; Yang, S.; Ju, T.-S.; Kim, C.; Chun, B. S.; Park, S.; Hwang, C. Universal method for magnetic skyrmion bubble generation by controlling the stripe domain instability. *NPG Asia Mater.* **2021**, *13* (1), 20.
(37) Jiang, W.; Chen, G.; Liu, K.; Zang, J.; te Velthuis, S. G. E.; Hoffmann, A. Skyrmions in magnetic multilayers. *Phys. Rep.* **2017**, *704*, 1−49.
(38) Choi, J.; Wu, J.; Won, C.; Wu, Y. Z.; Scholl, A.; Doran, A.; Owens, T.; Qiu, Z. Q. Magnetic bubble domain phase at the spin reorientation transition of ultrathin Fe/Ni/Cu(001) film. *Phys. Rev. Lett.* **2007**, *98* (20), 207205.
(39) Saratz, N.; Lichtenberger, A.; Portmann, O.; Ramsperger, U.; Vindigni, A.; Pescia, D. Experimental phase diagram of perpendicularly magnetized ultrathin ferromagnetic films. *Phys. Rev. Lett.* **2010**, *104* (7), 077203.
(40) Je, S. G.; Han, H. S.; Kim, S. K.; Montoya, S. A.; Chao, W.; Hong, I. S.; Fullerton, E. E.; Lee, K. S.; Lee, K. J.; Im, M. Y.; et al. Direct Demonstration of Topological Stability of Magnetic Skyrmions via Topology Manipulation. *ACS Nano* **2020**, *14* (3), 3251−3258.
(41) Je, S. G.; Vallobra, P.; Srivastava, T.; Rojas-Sanchez, J. C.; Pham, T. H.; Hehn, M.; Malinowski, G.; Baraduc, C.; Auffret, S.; Gaudin, G.; et al. Creation of Magnetic Skyrmion Bubble Lattices by Ultrafast Laser in Ultrathin Films. *Nano Lett.* **2018**, *18* (11), 7362−7371.
(42) Wang, Z.; Guo, M.; Zhou, H.-A.; Zhao, L.; Xu, T.; Tomasello, R.; Bai, H.; Dong, Y.; Je, S.-G.; Chao, W.; et al. Thermal generation, manipulation and thermoelectric detection of skyrmions. *Nat. Electron.* **2020**, *3* (11), 672−679.
(43) Kwon, H. Y.; Song, K. M.; Jeong, J.; Lee, A.-Y.; Park, S.-Y.; Kim, J.; Won, C.; Min, B.-C.; Chang, H. J.; Choi, J. W. High-density Néel-type magnetic skyrmion phase stabilized at high temperature. *NPG Asia Mater.* **2020**, *12* (1), 86.
(44) Woo, S.; Song, K. M.; Zhang, X.; Ezawa, M.; Zhou, Y.; Liu, X.; Weigand, M.; Finizio, S.; Raabe, J.; Park, M.-C.; et al. Deterministic creation and deletion of a single magnetic skyrmion observed by direct time-resolved X-ray microscopy. *Nat. Electron.* **2018**, *1* (5), 288−296.
(45) Finizio, S.; Zeissler, K.; Wintz, S.; Mayr, S.; Wessels, T.; Huxtable, A. J.; Burnell, G.; Marrows, C. H.; Raabe, J. Deterministic Field-Free Skyrmion Nucleation at a Nanoengineered Injector Device. *Nano Lett.* **2019**, *19* (10), 7246−7255.
(46) Ikeda, S.; Miura, K.; Yamamoto, H.; Mizunuma, K.; Gan, H. D.; Endo, M.; Kanai, S.; Hayakawa, J.; Matsukura, F.; Ohno, H. A perpendicular-anisotropy CoFeB-MgO magnetic tunnel junction. *Nat. Mater.* **2010**, *9* (9), 721−724.
(47) Yang, H. X.; Chshiev, M.; Dieny, B.; Lee, J. H.; Manchon, A.; Shin, K. H. First-principles investigation of the very large perpendicular magnetic anisotropy at FeIMgO and CoIMgO interfaces. *Phys. Rev. B* **2011**, *84* (5), 054401.
(48) Buttner, F.; Lemesh, I.; Beach, G. S. D. Theory of isolated magnetic skyrmions: From fundamentals to room temperature applications. *Sci. Rep.* **2018**, *8* (1), 4464.
(49) Cannas, S. A.; Carubelli, M.; Billoni, O. V.; Stariolo, D. A. Inverse transition in a two-dimensional dipolar frustrated ferromagnet. *Phys. Rev. B* **2011**, *84* (1), 014404.
(50) Meier, T. N. G.; Kronseder, M.; Back, C. H. Domain-width model for perpendicularly magnetized systems with Dzyaloshinskii-Moriya interaction. *Phys. Rev. B* **2017**, *96* (14), 144408.
(51) Yang, S.; Moon, K.-W.; Ju, T.-S.; Kim, C.; Park, S.; Hwang, C. Universality of stripe domain width change by an in-plane magnetic field. *J. Magn. Magn. Mater.* **2021**, *539*, 168381.
(52) Wilson, M. N.; Butenko, A. B.; Bogdanov, A. N.; Monchesky, T. L. Chiral skyrmions in cubic helimagnet films: The role of uniaxial anisotropy. *Phys. Rev. B* **2014**, *89* (9), 094411.
(53) Saratz, N.; Ramsperger, U.; Vindigni, A.; Pescia, D. Irreversibility, reversibility, and thermal equilibrium in domain patterns of Fe films with perpendicular magnetization. *Phys. Rev. B* **2010**, *82* (18), 184416.

https://doi.org/10.1021/acs.nanolett.2c02268
Nano Lett. 2022, 22, 8430−8436